ARTICLE

doi:10.1038/nature09714

Cortical representations of olfactory input by trans-synaptic tracing

Kazunari Miyamichi[1], Fernando Amat[2], Farshid Moussavi[2], Chen Wang[3], Ian Wickersham[4]†, Nicholas R. Wall[4], Hiroki Taniguchi[5], Bosiljka Tasic[1], Z. Josh Huang[5], Zhigang He[3], Edward M. Callaway[4], Mark A. Horowitz[2] & Liqun Luo[1]

In the mouse, each class of olfactory receptor neurons expressing a given odorant receptor has convergent axonal projections to two specific glomeruli in the olfactory bulb, thereby creating an odour map. However, it is unclear how this map is represented in the olfactory cortex. Here we combine rabies-virus-dependent retrograde mono-trans-synaptic labelling with genetics to control the location, number and type of 'starter' cortical neurons, from which we trace their presynaptic neurons. We find that individual cortical neurons receive input from multiple mitral cells representing broadly distributed glomeruli. Different cortical areas represent the olfactory bulb input differently. For example, the cortical amygdala preferentially receives dorsal olfactory bulb input, whereas the piriform cortex samples the whole olfactory bulb without obvious bias. These differences probably reflect different functions of these cortical areas in mediating innate odour preference or associative memory. The trans-synaptic labelling method described here should be widely applicable to mapping connections throughout the mouse nervous system.

The functions of mammalian brains are based on the activity patterns of large numbers of interconnected neurons that form information processing circuits. Neural circuits consist of local connections—where pre- and postsynaptic partners reside within the same brain area—and long-distance connections, which link different areas. Local connections can be predicted by axon and dendrite reconstructions[1], and confirmed by physiological recording and stimulation methods[2]. Long-distance connections are more difficult to map, as commonly used methods can only trace bulk projections with a coarse resolution. Most methods cannot distinguish axons in passing from those that form synapses, or pinpoint the neuronal types to which connections are made[1,2]. Trans-synaptic tracers can potentially overcome these limitations[2]. Here we combine a retrograde rabies-virus-dependent mono-trans-synaptic labelling technique[3] with genetic control of the location, number and cell type of 'starter' neurons to trace their presynaptic partners. We systematically mapped long-distance connections between the first olfactory processing centre, the olfactory bulb, and its postsynaptic targets in the olfactory cortex including the anterior olfactory nucleus (AON), piriform cortex and amygdala (Supplementary Fig. 1).

Genetic control of trans-synaptic tracing

Rabies virus can cross synapses from postsynaptic to presynaptic neurons with high specificity[4], without notable defects in the morphology or physiology of infected neurons for extended periods of time[3,5]. Recent genetic modifications of rabies virus have permitted mono-trans-synaptic labelling[3]. Specifically, the rabies envelope glycoprotein (G) required for viral spread was replaced with a fluorescent marker[6]. Further, the virus was pseudotyped with EnvA, an avian virus envelope protein that lacks an endogenous receptor in mammals, and thus cannot infect wild-type mammalian cells. However, it can infect cells expressing the EnvA receptor TVA, and can subsequently produce infectious particles if TVA-expressing cells also express G to complement the *ΔG* rabies virus (Fig. 1a, bottom). The new viral particles can cross synapses to label presynaptic partners of starter neurons. As trans-synaptically infected neurons do not express G, the modified virus cannot spread from them to other neurons. Paired recordings in cultured brain slices support the efficacy and specificity of this strategy[3].

To extend this method to a limited number of starter cells of a defined type and at a precise location *in vivo*, we combined mouse genetics and viral infections (Fig. 1a, b). We created a transgenic mouse (*CAG-stop-tTA2*) that conditionally expresses the tetracycline transactivator tTA2 under the control of a ubiquitous *CAG* promoter only upon Cre-mediated excision of a transcriptional stop cassette. After crossing these mice with transgenic mice expressing the tamoxifen-inducible Cre (CreER), a small fraction of CreER$^+$ cells also express tTA2 following tamoxifen induction. We then used stereotactic injections to deliver into specific regions of the brain an adeno-associated virus (AAV) serotype 2 expressing three proteins: histone–GFP, TVA and G, under the control of a tetracycline-response element (*TRE*). Expression of TVA and G allows infected, tTA2$^+$ cells to be receptive to infection by the modified rabies virus, which we injected into the same location two weeks later. We define starter cells as those infected by both AAV and rabies virus, and therefore labelled by both histone–GFP and mCherry; their presynaptic partners are infected only by rabies virus and therefore express only mCherry.

We tested our strategy by using a ubiquitously expressing *actin-CreER*[7] in combination with *CAG-stop-tTA2* in the neocortex. Starter cells could be unambiguously identified by histone–GFP expression (Supplementary Fig. 2). In all but one case, we observed more than one starter cell (Supplementary Fig. 3 shows the example of a single starter cell). In a typical example, 35 starter cells in the motor cortex expressed histone–GFP and mCherry (Fig. 1c (3)), demonstrating that AAV and rabies virus can infect the same cells *in vivo*. In addition to many locally labelled cells (Fig. 1c (1)), mCherry$^+$ cells were

[1]HHMI/Department of Biology, Stanford University, Stanford, California 94305, USA. [2]Department of Electrical Engineering, Stanford University, Stanford, California 94305, USA. [3]Department of Neuroscience, Children's Hospital, Boston, Massachusetts 02115, USA. [4]Systems Neurobiology Laboratory, The Salk Institute for Biological Studies and Neurosciences Graduate Program, University of California, San Diego, La Jolla, California 92037, USA. [5]Cold Spring Harbor Laboratory, New York, New York 11724, USA. †Present address: HHMI/Department of Brain and Cognitive Sciences, Massachusetts Institute of Technology, Cambridge, Massachusetts 02139, USA.

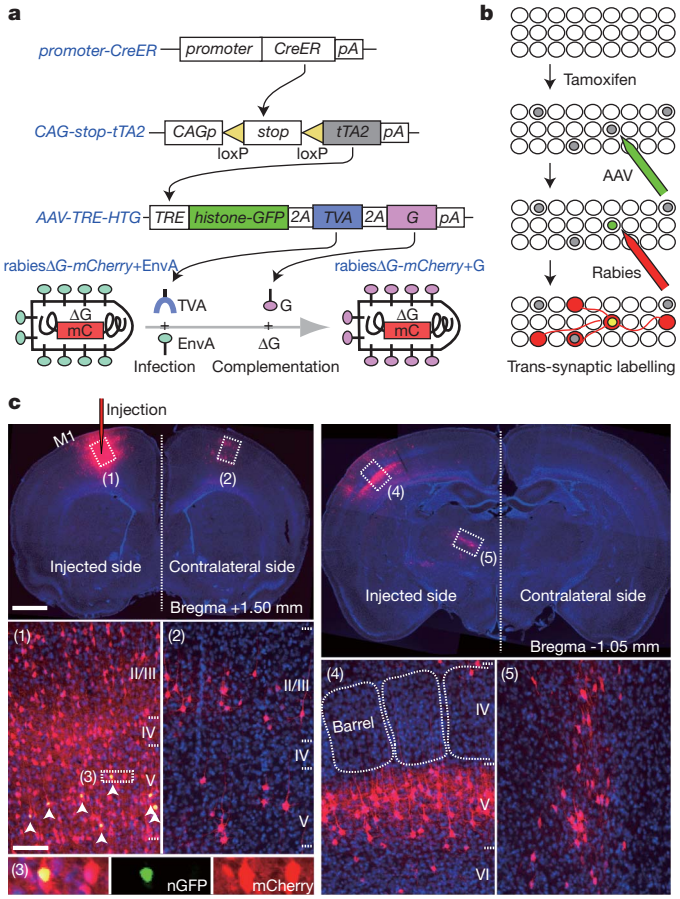

Figure 1 | Genetic control of rabies-mediated neural circuit tracing. **a**, **b**, Schematic representation of the methodology used to control the location, number and type of starter cells for rabies-virus-mediated trans-synaptic labelling. tTA2 is expressed in a small subset of CreER$^+$ cells (grey nuclei in **b**). tTA2 activates an AAV-delivered transgene to express: (1) a histone–GFP marker to label the nuclei of starter cells in green; (2) EnvA receptor (TVA) to enable subsequent infection by EnvA-pseudotyped rabies virus (rabies*ΔG-mCherry*+EnvA); and (3) rabies glycoprotein (G) to initiate trans-synaptic labelling. **c**, Top left, a 60-μm coronal section that includes the injection site in the motor cortex (M1). Cells labelled with both histone–GFP (nGFP) and mCherry (arrowheads in **c** (1), magnified in **c** (3)) can be distinguished from cells labelled with mCherry alone, which are found near the injection site (**c** (1)), in the contralateral motor cortex (**c** (2)), in the somatosensory barrel cortex (top right; magnified in **c** (4)), and in the motor-specific ventrolateral nucleus of the thalamus (**c** (5)). Scale bars, 1 mm for low-magnification images at the top, 100 μm for high-magnification images at the bottom.

enriched in layers II, III and V in the contralateral motor cortex (Fig. 1c (2)), consistent with layer specificity of callosal projections[8]. mCherry$^+$ cells were also found in layers III and V of the ipsilateral somatosensory cortex (Fig. 1c (4)) and in motor-specific thalamic nuclei (Fig. 1c (5)), which are known sources of monosynaptic inputs to the motor cortex[9].

In all experiments, histone–GFP$^+$ cells were found within 450 μm of the injection sites, consistent with a previous report that AAV serotype 2 predominantly infects neurons locally[10]. Omitting AAV or tamoxifen yielded no trans-synaptically labelled neurons (Supplementary Fig. 4). Moreover, our strategy labelled neurons only through synaptic connections but not through axons in passage (Supplementary Fig. 5). Finally, rabies virus spread was restricted to neurons directly connected to starter cells, and only in the retrograde direction (Supplementary Fig. 6). Together, these experiments validated our genetic strategy for retrograde mono-trans-synaptic labelling *in vivo*.

AON maintains the dorsal–ventral topography

In the mouse, olfactory receptor neurons that express a single type of odorant receptor send convergent axonal projections to a specific pair of glomeruli in the lateral and medial olfactory bulb[11–13]. Odorants are detected by combinations of olfactory receptor neuron classes[14], and are represented as spatiotemporal activity patterns of glomeruli[15]. Each mitral cell sends its apical dendrite to a single glomerulus and thus receives direct input from a single olfactory receptor neuron class. Mitral cell axons relay information to the olfactory cortex (Supplementary Fig. 1a). Previous axon tracing studies showed that individual mitral cells send axons to distinct cortical areas, and that small cortical regions receive broad input from the olfactory bulb[16–19]. However, understanding the principles underlying odour perception and odour-mediated behaviours requires systematic and quantitative analysis of connection patterns of mitral cells with their cortical target neurons.

We first established that mitral cells throughout the olfactory bulb can be infected by rabies virus via their axons (Supplementary Fig. 7). We then applied our strategy (Fig. 1a, b) to specific areas of the AON, piriform cortex and cortical amygdala (Supplementary Fig. 1b), and examined the distribution of trans-synaptically labelled mitral cells. In a typical example, 11 clustered starter cells in the AON (Fig. 2a) resulted in 69 labelled mitral cells distributed widely across the olfactory bulb (Supplementary Fig. 8 and Supplementary Movie 1). Bright mCherry fluorescence from rabies virus allowed us to unequivocally follow the primary dendrites of the labelled mitral cells to single target glomeruli (Fig. 2b). Each mitral cell sent its apical dendrite into a single glomerulus. Four glomeruli were each innervated by two labelled mitral cells (Fig. 2b, right, and Supplementary Table 1).

To quantitatively compare the patterns of labelled glomeruli from different animals, we established a three-dimensional (3D) reconstruction protocol for the olfactory bulb, and aligned each olfactory bulb to a standard olfactory bulb model (Fig. 2c). To test the accuracy of this procedure, we reconstructed and aligned olfactory bulbs from three *P2-IRES-tauGFP* transgenic mice[20]. These GFP-labelled glomeruli were located within a distance of a few glomeruli from each other (Supplementary Fig. 9), consistent with the natural variability of olfactory receptor neuron axon targeting[21]. This precision of our 3D reconstruction enables the comparison of olfactory bulbs from different animals.

The AON has been proposed to provide feedforward modification of information from the olfactory bulb to the piriform cortex[22]. Little is known about its organization except for a small and distinct AON pars externa, which maintains dorsal–ventral olfactory bulb topography[23–25]. We injected AAV and rabies virus to different areas of the AON (Supplementary Table 1), and established an AON 3D-reconstruction protocol analogous to that for the olfactory bulb (Fig. 2c, left). Labelled glomeruli from AON injections were distributed widely in the olfactory bulb (Fig. 2c, middle). However, starter cells from the ventral and dorsal AON preferentially labelled ventral and dorsal glomeruli, respectively (Fig. 2c). To quantify the spatial distributions of starter cells in the AON and trans-synaptically labelled glomeruli in the olfactory bulb, we introduced a cylindrical coordinate system into the olfactory bulb and AON models, where Z represents the position along the anterior–posterior axis and θ represents the angle from the polar axis (Fig. 2c). No correlations were found between Z_{AON} and θ_{OB} (where OB is olfactory bulb), Z_{AON} and Z_{OB}, or θ_{AON} and Z_{OB} (Supplementary Fig. 10a). However, we found a strong positive correlation ($R^2 = 0.79$) between θ_{AON} and θ_{OB} (Fig. 2d), which correspond to the dorsal–ventral axes of the AON and olfactory bulb, respectively. Thus, the AON maintains the dorsal–ventral topography of the olfactory bulb.

A coarse topography exists between olfactory receptor neuron cell-body positions in the olfactory epithelium and target glomeruli in the olfactory bulb along the dorsal–ventral axis[26]. Specifically, the olfactory cell adhesion molecule (OCAM) is expressed in a subset of olfactory receptor neurons[27] that project to the ventral ~55% of glomeruli in the olfactory bulb. In the olfactory bulb, ~25° clockwise rotation of the

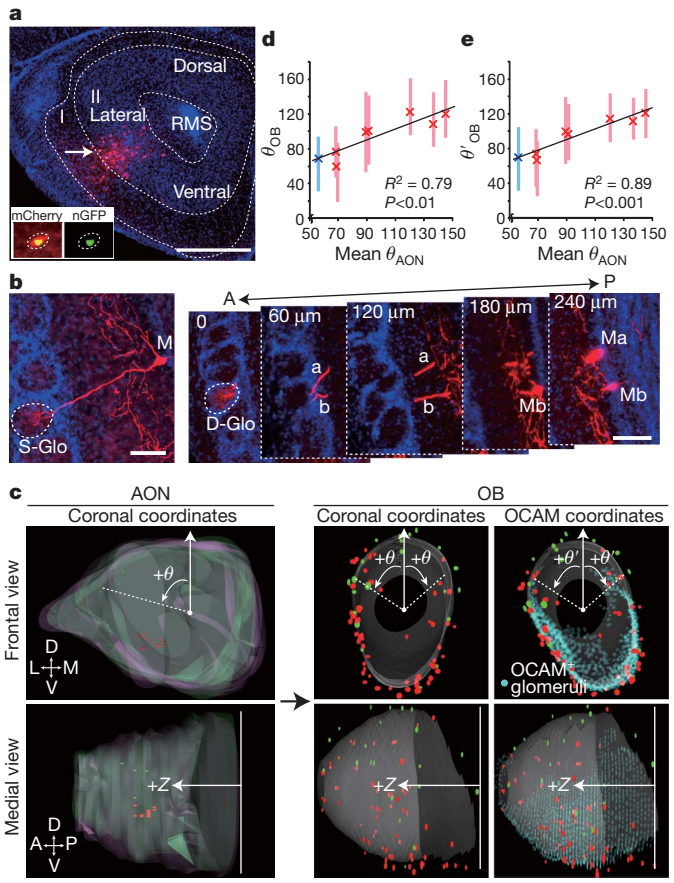

Figure 2 | The olfactory bulb to AON connections show a dorsal–ventral topography. a, A 60-µm coronal section with two starter cells located in layer II of the ventrolateral AON, one of which (arrow) is magnified in the inset. RMS, rostral migratory stream. Scale bar, 500 µm. **b**, Typical examples of trans-synaptically labelled mitral cells from cortical starter cells. Left, a 60-µm coronal section that captures both the cell body and the apical dendrite of a mitral cell. Right, more frequently, a mitral cell apical dendrite spans several consecutive 60-µm coronal sections. S-Glo, glomerulus innervated by a single labelled mitral cell (M). D-Glo, glomerulus innervated by two labelled mitral cells (Ma, Mb). A, anterior; P, posterior. Scale bar, 100 µm. **c**, Superimposed 3D reconstructions of the AONs and olfactory bulbs (OBs) from two injected brains. Eleven red and four green starter cells from two AONs labelled red and green glomeruli, respectively. Light red and green, contours of two superimposed AONs. D, dorsal; L, lateral; M, medial, V, ventral. **d**, **e**, Correlations between θ_{AON} and θ_{OB} (**d**) and θ_{AON} and θ'_{OB} (**e**). Crosses represent mean θ_{AON} (x-axis) and mean θ_{OB} or θ'_{OB} (y-axis). Error bars represent 50% of the distribution surrounding the mean θ_{OB} or θ'_{OB}. R^2, square of Pearson's correlation coefficient; P, statistical significance tested against the null hypothesis assuming no correlation between θ_{AON} and θ_{OB} or θ'_{OB}. Red and blue, experiments using *actin-CreER* and *CaMKII-CreER*[47], respectively.

polar axis around the z-axis maximized the separation of OCAM$^+$ and OCAM$^-$ glomeruli (Supplementary Fig. 11). In this new OCAM coordinate system represented by θ'_{OB} (Fig. 2c, right), the correlation coefficient between θ'_{OB} and θ_{AON} increased to $R^2 = 0.89$ (Fig. 2e), showing that adjusting the dorsal–ventral axis of the olfactory bulb according to a biological marker improved the AON and olfactory bulb topographic correspondence. Thus, the topography between the olfactory epithelium and the olfactory bulb further extends to the AON.

Dorsally biased olfactory bulb input to amygdala

Mitral cell axons project to the anterior and posterolateral cortical amygdala[28,29]. The organization of this axonal input is unknown. We injected AAV and rabies virus to small areas within these regions, and mapped starter cells onto a common schematic drawing based on anatomical landmarks (Fig. 3a). Trans-synaptically labelled mitral cells and glomeruli from amygdala starter cells were broadly distributed in the olfactory bulb. However, the labelled glomeruli were enriched in the dorsal olfactory bulb (Fig. 3c). For quantification, we compared the mean experimental θ'_{OB} for each injection with mean θ'_{OB} values produced by computer simulation from the same number of glomeruli distributed randomly throughout the olfactory bulb ($^{sim}\theta'_{OB}$). For the AON experiments, the mean experimental θ'_{OB} values for the majority of the samples were significantly larger or smaller than the corresponding mean $^{sim}\theta'_{OB}$ values (Fig. 3e, left), reflecting the dorsal–ventral topography between the olfactory bulb and the AON. By contrast, none of the mean θ'_{OB} values from the amygdala was significantly larger than the corresponding mean $^{sim}\theta'_{OB}$ (Fig. 3e, middle). Six out of ten mean θ'_{OB} values from the cortical amygdala fell significantly below the corresponding mean $^{sim}\theta'_{OB}$ values. For these dorsally biased samples, the density of labelled glomeruli gradually decreased along the dorsal–ventral axis without a sharp boundary (Supplementary Fig. 12). Simple spatial correspondence between starter-cell locations and the degree of dorsal bias was not evident (Supplementary Fig. 10b). In summary, the cortical amygdala overall receives biased input from the dorsal olfactory bulb.

Less organized olfactory bulb input to piriform cortex

The piriform cortex is the largest cortical area in the olfactory cortex. Recent physiological analysis[30,31] found that neurons activated by specific odours are apparently not spatially organized; the underlying anatomical basis is unclear. We injected AAV and rabies virus into several areas in the anterior and posterior piriform cortex, and mapped starter cells from different brains onto a common schematic drawing of the entire piriform cortex based on anatomical landmarks (Fig. 3b). Labelled glomeruli were broadly distributed throughout the olfactory bulb, regardless of starter-cell locations in the piriform cortex (Fig. 3d). In sharp contrast to trans-synaptic labelling from the AON or amygdala, where different samples showed highly variable mean θ'_{OB}, mean θ'_{OB} values from the piriform cortex tracings were much less variable and closely resembled a random distribution (Fig. 3e). Only one out of ten samples had a mean θ'_{OB} slightly above the 95th percentile of the mean $^{sim}\theta'_{OB}$. Further, no strong spatial correspondence was evident in correlation analyses of θ'_{OB}, Z_{OB} and the location of starter cells in the piriform cortex (Supplementary Fig. 10c). These data indicate that highly restricted areas of the piriform cortex receive direct mitral cell input representing glomeruli that are distributed throughout the olfactory bulb with no apparent spatial organization.

Convergence of mitral cell input

Convergent inputs from different glomeruli to individual cortical neurons could allow the olfactory cortex to integrate combinatorial odour representations in the olfactory bulb. In support of this, previous studies have shown that odour receptive ranges of AON cells are broader than those of mitral cells[32], and that some piriform cortex neurons are activated by a binary odour mix but not individual components[31]. However, a large fraction of inputs in these studies could come from other cortical neurons through extensive recurrent connections (Figs 2a and 3a, b). Direct convergence of mitral cell axons onto individual cortical neurons is implied in physiological studies of piriform cortical neurons in slices[33–35]. Our trans-synaptic labelling enabled a direct examination of mitral cell convergence to individual cortical neurons *in vivo*.

The convergence index, defined by the number of labelled mitral cells divided by the number of the starter cells in the cortex, exceeded 1 in all experiments using *actin-CreER* (Fig. 4a and Supplementary Table 1). This finding demonstrates that individual cortical neurons receive direct inputs from multiple mitral cells *in vivo*. As the vast majority of labelled mitral cells corresponded to different glomeruli (Supplementary Table 1), individual cortical neurons must receive direct inputs representing multiple glomeruli. This convergence index

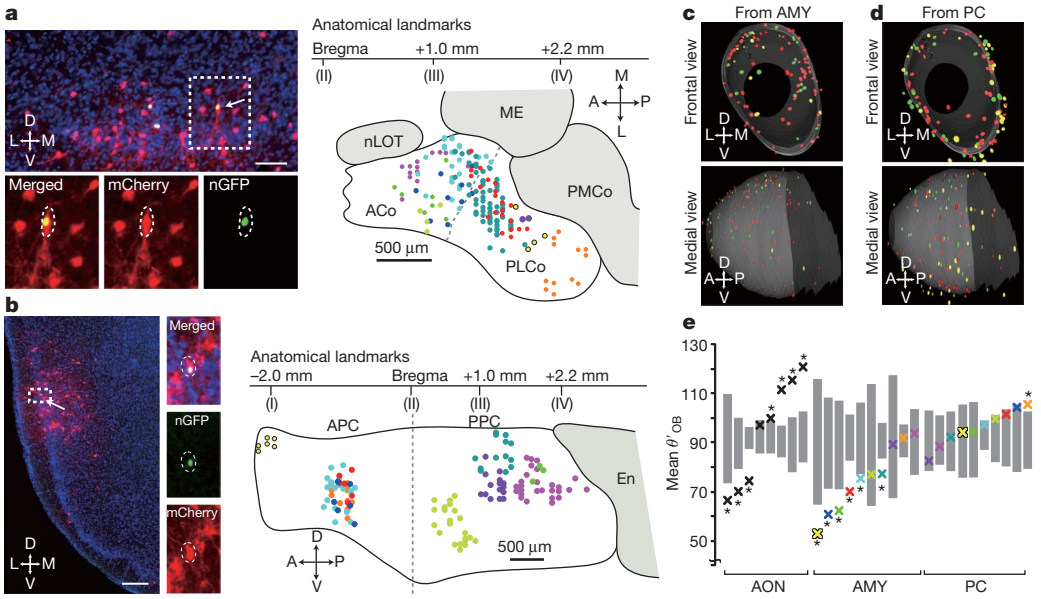

Figure 3 | Representations of olfactory bulb input in the amygdala and piriform cortex. **a**, **b**, Starter cells from the cortical amygdala and piriform cortex. Left, single coronal sections at the injection sites in the posterolateral cortical amygdala (**a**) and the posterior piriform cortex (**b**). Arrows point to starter cells magnified in insets. Scale bars, 100 µm in **a**, 200 µm in **b**. Right, schematic representations of ten independent injections each into amygdala (**a**) or piriform cortex (**b**). Starter cells from each injection are labelled with a specific colour. The dotted line denotes the rough border between the anterior cortical amygdala (ACo) and the posterolateral cortical amygdala (PLCo) based on anatomical landmarks according to a mouse brain atlas[48]. APC, anterior piriform cortex; En, lateral entorhinal cortex; ME, medial amygdala; nLOT, nucleus of lateral olfactory tract; PMCo, posteromedial cortical amygdala; PPC, posterior piriform cortex. **c**, **d**, Superposition of three independent 3D reconstructions of glomerular maps with starter cells from the cortical amygdala (AMY; **c**) or the piriform cortex (PC; **d**). **e**, Mean θ'_{OB} values (crosses) from each experiment are plotted in the same column with the 95% confidence intervals for corresponding ${}^{sim}\theta'_{OB}$ values (grey bars). Samples with experimental mean θ'_{OB} outside the 95% confidence intervals are labelled with asterisks ($^*P < 0.05$). Colours in **a** (scheme), **c** and **e** (amygdala) are matched to represent the same samples, and so are the colours in **b** (scheme), **d** and **e** (piriform cortex).

is probably an underestimate, as not all starter cells necessarily received direct mitral cell input (overestimation of the denominator), and not all cells presynaptic to starter cells were trans-synaptically infected by the rabies virus (underestimation of the numerator; see Supplementary Fig. 3).

The convergence indices varied widely in different experiments, and did not differ substantially in the three cortical areas we examined. However, in experiments that contained starter cells located in layer I, which is mostly composed of GABAergic local interneurons[36], the convergence indices were greater (Fig. 4a, red). Assuming all starter cells in a given layer contribute equally to mitral cell labelling, multiple regression analyses indicate that layer I neurons receive direct input from more mitral cells than layer II/III neurons (Fig. 4b).

To confirm the higher convergence index for layer I GABAergic neurons, we replaced the ubiquitous *actin-CreER* with *GAD2-CreER*, which is expressed only in GABAergic interneurons (Supplementary Fig. 13). We found that GABAergic neurons located in layer II or III of the piriform cortex received little direct mitral cell input, whereas those located in layer I showed a much greater convergence index (Fig. 4b, right, and Supplementary Table 1). Thus, cortical GABAergic neurons are highly diverse with respect to mitral cell innervation. These observations are in accordance with recent physiological studies[30,34], and suggest different physiological roles for these GABAergic neurons; layer I and deeper layer GABAergic neurons provide global feedforward and feedback inhibition to cortical pyramidal neurons, respectively.

Sister mitral cells connect independently

Each glomerulus is innervated by the apical dendrites of ~25 electrically coupled mitral cells[37]. We refer to these cells as 'sister' mitral cells. Sister mitral cells may preferentially connect to the same cortical postsynaptic target neurons compared to 'non-sister' mitral cells that receive direct input from different glomeruli. Such an organization could increase the signal-to-noise ratio in information transmission from mitral cells to cortical neurons. Alternatively, sister mitral cells may connect to cortical neurons independently to deliver olfactory information widely across different cortical neurons.

We used the frequency of dually labelled glomeruli from our data set and statistical simulation to distinguish between these possibilities. Dually labelled glomeruli (D) could result from a single starter cell (Ds) or two starter cells (Dt). Assuming that an individual starter cell can receive input from any of the 2,000 glomeruli, we compared the distribution of Ds derived from our data and from a simulation according to the null hypothesis that sister mitral cells connect independently with postsynaptic targets. If sister mitral cells share significantly more postsynaptic targets than at random, then the 'data Ds' distribution should be significantly higher than the simulated 'random Ds' distribution. In all but two cases, these two distributions were not statistically different (Fig. 4c). Both exceptions came from trans-synaptic labelling from the AON, which showed dorsal–ventral topography, so the original assumptions were not accurate. When we reduced the number of accessible glomeruli to 1,500, no sample showed significant differences. Thus, our analysis indicates that individual mitral cells innervating the same glomerulus act independently in making connections with their cortical targets.

Discussion

Our study revealed several general principles that define cortical representations of the olfactory bulb input. First, individual cortical neurons receive direct input from mitral cells originating from multiple glomeruli. On average, each excitatory neuron receives direct input from four mitral cells, but this number is likely to be an underestimate. Convergence of mitral cell inputs enables cortical neurons to integrate information from discrete olfactory channels. The lower bound of four already affords $\sim 10^{12}$ glomerular combinations for 1,000 olfactory channels, far exceeding the number of neurons in the mouse olfactory cortex. Thus, the olfactory cortical neuron repertoire samples only a

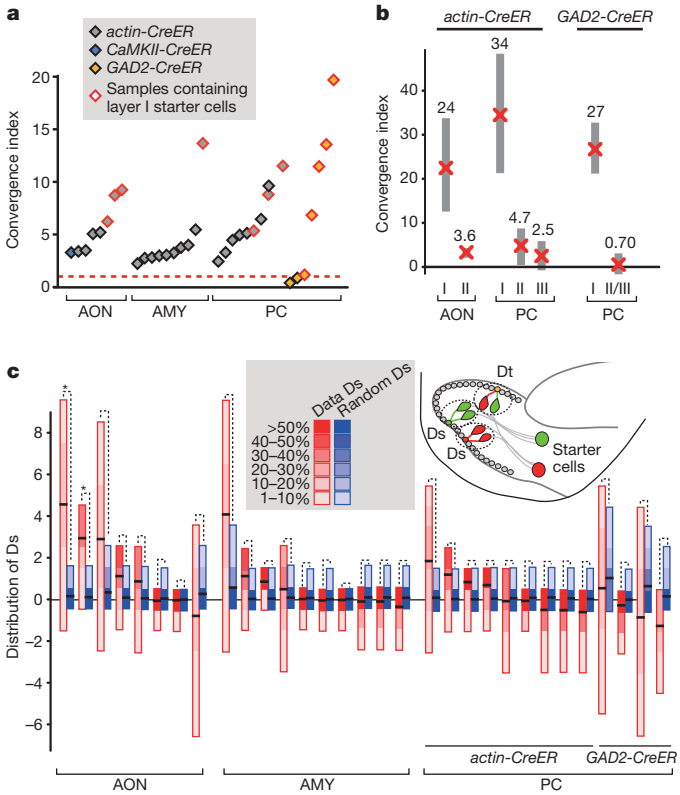

Figure 4 | Convergence and independence of mitral cell inputs. **a**, Convergence index for each cortical injection experiment is represented by a diamond, with the type and layer of starter cells specified by the colour code above. AMY, amygdala; PC, piriform cortex. **b**, Multiple regression analysis to estimate the convergence indices of starter cells located in different layers of the AON and piriform cortex. Estimated mean convergence indices (red crosses) and the corresponding 95% confidence intervals (grey bars) are shown. Data from *actin-CreER* and *GAD2-CreER* were analysed separately. Injections into amygdala produced only one sample that contained layer I cells and were therefore excluded. **c**, Schematic of dually labelled glomeruli (D) resulting from two starter cells (Dt) or a single starter cell (Ds). Comparison of the distributions of Ds derived from experimentally observed frequency of D (Data Ds; red) and from simulated D based on the null hypothesis detailed in Methods (Random Ds; blue). For each sample, the distributions of 'data Ds' and 'random Ds' are shown by coloured heat maps. $*P < 0.05$.

small fraction of all possible combinations of direct olfactory bulb inputs.

Second, neurons restricted to small olfactory cortical regions receive input from glomeruli that are broadly distributed in the olfactory bulb. Although similar findings were reported previously[16–19], our study provides a higher resolution analysis of direct connectivity between mitral cells and cortical neurons, rather than inferring connection from the presence of axons, which could be a major caveat of previous tracing studies (see Supplementary Fig. 5). At the same time, mitral cells representing the same glomerulus connect independently to post-synaptic cortical neurons, thus maximizing the spread of olfactory information originating from individual olfactory channels. Our finding is consistent with analyses of axon arborization patterns of singly labelled mitral cells (S. Ghosh and colleagues; manuscript submitted).

Third, different cortical areas receive differentially organized olfactory bulb input (Supplementary Fig. 1c). The AON maintains a coarse topography along the dorsal–ventral axis, suggesting a pre-processing role for olfactory-bulb-derived information before sending to other cortical areas. A lack of apparent spatial organization in the piriform cortex with regard to olfactory bulb input provides an anatomical basis for recent physiological studies[30,31], and suggests that the piriform cortex acts as an association cortex[31,38]. In the cortical amygdala, many neurons seem to receive strongly biased input from the dorsal olfactory bulb. Mice lacking olfactory receptor neurons that project to the dorsal olfactory bulb lose their innate avoidance of odours from predator urine and spoiled food, despite retaining the ability to sense these odours[39]. The cortical amygdala may preferentially process the olfactory information that directs innate behaviours. Our study is in agreement with similar findings using axon tracings from individual glomeruli (D. L. Sosulski and colleagues; manuscript submitted).

Interestingly, axonal arborization patterns of *Drosophila* olfactory projection neurons (equivalent to mitral cells) in higher olfactory centres show a similar organizational principle. Projection neuron axon arborization patterns in the lateral horn—a processing centre directing odour-mediated innate behaviour—are highly stereotyped with respect to projection neuron classes[40,41], and are partitioned according to the biological significance of the odorants[42]. Arborization patterns of axon collaterals of the same projection neurons in the mushroom body, an olfactory memory centre[43], are much less stereotyped[40,42], consistent with a physiological study indicating non-stereotyped connections[44]. Therefore, from insects to mammals, a common theme emerges for the representations of olfactory information: more stereotyped and selective representation of odours is necessary for directing innate behaviours, whereas broader and less stereotyped sampling of the whole olfactory space is better suited for brain regions implicated in associative memories.

The genetically controlled mono-trans-synaptic tracing described here should be widely applicable for mapping neuronal circuitry throughout the mouse brain. It is currently unknown how rabies virus crosses synapses, and whether the efficiency and specificity vary with cell type, connection strength and activity[3,5,45]. Further applications of these trans-synaptic methods to other neurons and circuits[46] will be necessary to address these questions. Nevertheless, the control experiments (Fig. 1 and Supplementary Figs 2–6) confirmed that our strategy labels neurons that are directly presynaptic to starter cells but not neurons whose axons pass through the injection sites without making synapses. Our method will be especially valuable for analysing long-distance connections that are usually refractory to physiological mapping strategies[2]. This method can be further extended to genetic manipulation of starter cells to combine circuit tracing with genetic loss- or gain-of-function experiments. These approaches will facilitate the investigation of not only the organization of information flow within neural circuits, but also the molecular basis of neuronal connections at single-cell resolution *in vivo*.

METHODS SUMMARY

Detailed methods on the generation of *CAG-stop-tTA2* mice, viral preparations, animal surgery, tissue processing, 3D reconstruction and quantitative analyses can be found in Methods.

Full Methods and any associated references are available in the online version of the paper at www.nature.com/nature.

Received 23 August; accepted 2 December 2010.
Published online 22 December 2010.

1. Cowan, W. M. The emergence of modern neuroanatomy and developmental neurobiology. *Neuron* **20,** 413–426 (1998).
2. Luo, L., Callaway, E. M. & Svoboda, K. Genetic dissection of neural circuits. *Neuron* **57,** 634–660 (2008).
3. Wickersham, I. R. *et al.* Monosynaptic restriction of transsynaptic tracing from single, genetically targeted neurons. *Neuron* **53,** 639–647 (2007).
4. Ugolini, G. Specificity of rabies virus as a transneuronal tracer of motor networks: transfer from hypoglossal motoneurons to connected second-order and higher order central nervous system cell groups. *J. Comp. Neurol.* **356,** 457–480 (1995).
5. Ugolini, G. Advances in viral transneuronal tracing. *J. Neurosci. Methods* **194,** 2–20 (2010).
6. Wickersham, I. R., Finke, S., Conzelmann, K. K. & Callaway, E. M. Retrograde neuronal tracing with a deletion-mutant rabies virus. *Nature Methods* **4,** 47–49 (2007).
7. Guo, C., Yang, W. & Lobe, C. G. A Cre recombinase transgene with mosaic, widespread tamoxifen-inducible action. *Genesis* **32,** 8–18 (2002).
8. Wise, S. P. & Jones, E. G. The organization and postnatal development of the commissural projection of the rat somatic sensory cortex. *J. Comp. Neurol.* **168,** 313–343 (1976).

9. Iriki, A., Pavlides, C., Keller, A. & Asanuma, H. Long-term potentiation in the motor cortex. *Science* **245,** 1385–1387 (1989).
10. Taymans, J. M. *et al.* Comparative analysis of adeno-associated viral vector serotypes 1, 2, 5, 7, and 8 in mouse brain. *Hum. Gene Ther.* **18,** 195–206 (2007).
11. Vassar, R. *et al.* Topographic organization of sensory projections to the olfactory bulb. *Cell* **79,** 981–991 (1994).
12. Ressler, K. J., Sullivan, S. L. & Buck, L. B. Information coding in the olfactory system: evidence for a stereotyped and highly organized epitope map in the olfactory bulb. *Cell* **79,** 1245–1255 (1994).
13. Mombaerts, P. *et al.* Visualizing an olfactory sensory map. *Cell* **87,** 675–686 (1996).
14. Malnic, B., Hirono, J., Sato, T. & Buck, L. B. Combinatorial receptor codes for odors. *Cell* **96,** 713–723 (1999).
15. Wilson, R. I. & Mainen, Z. F. Early events in olfactory processing. *Annu. Rev. Neurosci.* **29,** 163–201 (2006).
16. Luskin, M. B. & Price, J. L. The distribution of axon collaterals from the olfactory bulb and the nucleus of the horizontal limb of the diagonal band to the olfactory cortex, demonstrated by double retrograde labeling techniques. *J. Comp. Neurol.* **209,** 249–263 (1982).
17. Scott, J. W., McBride, R. L. & Schneider, S. P. The organization of projections from the olfactory bulb to the piriform cortex and olfactory tubercle in the rat. *J. Comp. Neurol.* **194,** 519–534 (1980).
18. Shipley, M. T. & Adamek, G. D. The connections of the mouse olfactory bulb: a study using orthograde and retrograde transport of wheat germ agglutinin conjugated to horseradish peroxidase. *Brain Res. Bull.* **12,** 669–688 (1984).
19. Nevelle, K. R. & Haberly, L. B. in *The Synaptic Organization of the Brain* (ed. Shepherd, G. M.) (Oxford Univ. Press, 2004).
20. Feinstein, P. & Mombaerts, P. A contextual model for axonal sorting into glomeruli in the mouse olfactory system. *Cell* **117,** 817–831 (2004).
21. Schaefer, M. L., Finger, T. E. & Restrepo, D. Variability of position of the P2 glomerulus within a map of the mouse olfactory bulb. *J. Comp. Neurol.* **436,** 351–362 (2001).
22. Brunjes, P. C., Illig, K. R. & Meyer, E. A. A field guide to the anterior olfactory nucleus (cortex). *Brain Res. Rev.* **50,** 305–335 (2005).
23. Yan, Z. *et al.* Precise circuitry links bilaterally symmetric olfactory maps. *Neuron* **58,** 613–624 (2008).
24. Schoenfeld, T. A. & Macrides, F. Topographic organization of connections between the main olfactory bulb and pars externa of the anterior olfactory nucleus in the hamster. *J. Comp. Neurol.* **227,** 121–135 (1984).
25. Scott, J. W., Ranier, E. C., Pemberton, J. L., Orona, E. & Mouradian, L. E. Pattern of rat olfactory bulb mitral and tufted cell connections to the anterior olfactory nucleus pars externa. *J. Comp. Neurol.* **242,** 415–424 (1985).
26. Miyamichi, K., Serizawa, S., Kimura, H. M. & Sakano, H. Continuous and overlapping expression domains of odorant receptor genes in the olfactory epithelium determine the dorsal/ventral positioning of glomeruli in the olfactory bulb. *J. Neurosci.* **25,** 3586–3592 (2005).
27. Yoshihara, Y. *et al.* OCAM: a new member of the neural cell adhesion molecule family related to zone-to-zone projection of olfactory and vomeronasal axons. *J. Neurosci.* **17,** 5830–5842 (1997).
28. Swanson, L. W. & Petrovich, G. D. What is the amygdala? *Trends Neurosci.* **21,** 323–331 (1998).
29. Scalia, F. & Winans, S. S. The differential projections of the olfactory bulb and accessory olfactory bulb in mammals. *J. Comp. Neurol.* **161,** 31–55 (1975).
30. Poo, C. & Isaacson, J. S. Odor representations in olfactory cortex: "sparse" coding, global inhibition, and oscillations. *Neuron* **62,** 850–861 (2009).
31. Stettler, D. D. & Axel, R. Representations of odor in the piriform cortex. *Neuron* **63,** 854–864 (2009).
32. Lei, H., Mooney, R. & Katz, L. C. Synaptic integration of olfactory information in mouse anterior olfactory nucleus. *J. Neurosci.* **26,** 12023–12032 (2006).
33. Franks, K. M. & Isaacson, J. S. Strong single-fiber sensory inputs to olfactory cortex: implications for olfactory coding. *Neuron* **49,** 357–363 (2006).
34. Stokes, C. C. & Isaacson, J. S. From dendrite to soma: dynamic routing of inhibition by complementary interneuron microcircuits in olfactory cortex. *Neuron* **67,** 452–465 (2010).
35. Apicella, A., Yuan, Q., Scanziani, M. & Isaacson, J. S. Pyramidal cells in piriform cortex receive convergent input from distinct olfactory bulb glomeruli. *J. Neurosci.* **30,** 14255–14260 (2010).
36. Suzuki, N. & Bekkers, J. M. Inhibitory neurons in the anterior piriform cortex of the mouse: classification using molecular markers. *J. Comp. Neurol.* **518,** 1670–1687 (2010).
37. Christie, J. M. *et al.* Connexin36 mediates spike synchrony in olfactory bulb glomeruli. *Neuron* **46,** 761–772 (2005).
38. Haberly, L. B. Parallel-distributed processing in olfactory cortex: new insights from morphological and physiological analysis of neuronal circuitry. *Chem. Senses* **26,** 551–576 (2001).
39. Kobayakawa, K. *et al.* Innate versus learned odour processing in the mouse olfactory bulb. *Nature* **450,** 503–508 (2007).
40. Marin, E. C., Jefferis, G. S., Komiyama, T., Zhu, H. & Luo, L. Representation of the glomerular olfactory map in the *Drosophila* brain. *Cell* **109,** 243–255 (2002).
41. Wong, A. M., Wang, J. W. & Axel, R. Spatial representation of the glomerular map in the *Drosophila* protocerebrum. *Cell* **109,** 229–241 (2002).
42. Jefferis, G. S. *et al.* Comprehensive maps of *Drosophila* higher olfactory centers: spatially segregated fruit and pheromone representation. *Cell* **128,** 1187–1203 (2007).
43. Davis, R. L. Olfactory memory formation in *Drosophila*: from molecular to systems neuroscience. *Annu. Rev. Neurosci.* **28,** 275–302 (2005).
44. Murthy, M., Fiete, I. & Laurent, G. Testing odor response stereotypy in the *Drosophila* mushroom body. *Neuron* **59,** 1009–1023 (2008).
45. Marshel, J. H., Mori, T., Nielsen, K. J. & Callaway, E. M. Targeting single neuronal networks for gene expression and cell labeling *in vivo*. *Neuron* **67,** 562–574 (2010).
46. Stepien, A. E., Tripodi, M. & Arber, S. Monosynaptic rabies virus reveals premotor network organization and synaptic specificity of cholinergic partition cells. *Neuron* **68,** 456–472 (2010).
47. Madisen, L. *et al.* A robust and high-throughput Cre reporting and characterization system for the whole mouse brain. *Nature Neurosci.* **13,** 133–140 (2010).
48. Lein, E. S. *et al.* Genome-wide atlas of gene expression in the adult mouse brain. *Nature* **445,** 168–176 (2007).

Supplementary Information is linked to the online version of the paper at www.nature.com/nature.

Acknowledgements We thank Stanford Transgenic Facility for help in generating transgenic mice, F. Zhang and K. Deisseroth for teaching us stereotactic injection, Y. Yoshihara and H. Zeng for reagents, C. Manalac and M. Shu for technical assistance, R. Axel, L. Buck, and L. Stryer, R. Yuste and members of the L.L. laboratory for discussion and critical reading of the manuscript. K.M. was supported by the JSPS program for Research Abroad and Human Frontier Science Program. K.M. is currently a research associate and L.L. is an investigator of the Howard Hughes Medical Institute. This work was also supported by an NIH grant.

Author Contributions K.M. planned and performed all the experiments. F.A. and F.M. developed the computer programs for 3D reconstructions and statistical simulation under the supervision of M.A.H. C.W. and Z.H. performed the initial AAV production. I.W., N.R.W. and E.M.C. provided the modified rabies virus and the construct to make the AAV vector. H.T. and Z.J.H. provided the *GAD2-CreER* mice. B.T. provided DNA constructs. L.L. supervised the project. L.L. and K.M. wrote the manuscript, with contributions from B.T.

Author Information Reprints and permissions information is available at www.nature.com/reprints. The authors declare no competing financial interests. Readers are welcome to comment on the online version of this article at www.nature.com/nature. Correspondence and requests for materials should be addressed to L.L. (lluo@stanford.edu).

METHODS

Generation of *CAG-stop-tTA2* Mice. The *tTA2* transactivator gene[49] was placed after the *CAG* promoter of plasmid *pCA-HZ2* (ref. 50) using a polymerase chain reaction (PCR)-based cloning method. A neomycin resistance (*neo*^{r}) gene and a transcriptional stop signal[51] were flanked by *loxP* sites to create a *loxP-neo*^{r}*-stop-loxP* cassette. This cassette was then introduced between the *CAG* promoter and *tTA2* using PCR-based cloning. An EcoRI fragment obtained from *ETLpA-/LTNL*[13], which contains the *IRES-tau-lacZ* cassette, was introduced after the *tTA2* coding sequence. The resulting cassette (*CAG-stop-tTA2-IRES-tau-lacZ*) was cloned into *pBT264* to flank the cassette with two copies of a ~250-bp β-globin *HS4* insulator sequence[52] on each side. *pBT264* (*pii-TRE-tdTomato-3Myc-ii*) was generated by inserting PCR-amplified copies of ~250-bp-long core insulator fragments (*i*) from the chicken β-globin HS4 insulator on each side of *TRE-tdTomato-3Myc* in *pBT239*. The insulator fragments were amplified from *pJC13-1* (ref. 53). The final construct, *pKM1* (*pii-CAG-stop-tTA2-IRES-tau-lacZii*), was tested by transient co-transfection with *pBT264* into cultured HEK293 cells. When a Cre-encoding plasmid *pBT140* (cytomegalovirus (CMV) promoter driving nuclear localization signal-*Cre*) was further introduced into the same cell, strong tdTomato fluorescence was detected 72 h after transfection. *pKM2* was digested with restriction enzymes SwaI and AscI, the insert was gel-purified using Qiagen gel extraction kit and eluted into 10 mM Tris-HCl, pH 7.4, 0.1 mM EDTA. The purified and linearized DNA devoid of plasmid backbone was used for mouse transgenesis via standard pronuclear injection procedure. Founders were screened by PCR primers to detect the *neo*^{r} gene. Four independent transgenic lines were established. They were crossed with mice containing *β-actin-CreER*[7] and *TRE-Bi-SG-T* reporter[53] to screen for functional *CAG-stop-tTA2* transgenes. Mice containing all three transgenes were injected with 1 mg of tamoxifen in corn oil at postnatal day (PD)10, and brains were collected at PD21 for the analysis. Two lines showed broad tdTomato fluorescence throughout the brain. One line (containing 2–3 copies of the transgene based on Southern blotting) was used exclusively in this study.

Virus preparations. All viral procedures followed the Biosafety Guidelines approved by the Stanford University Administrative Panel on Laboratory Animal Care (A-PLAC) and Administrative Panel of Biosafety (APB). To make the AAV containing the *TRE-HTG* cassette, which encodes histone–GFP, TVA and G linked by the 2A 'self-cleaving' peptides, the *HTG* cassette obtained from *pBOB-synP-HTB* (I.W. and E.M.C., unpublished plasmid) was placed after the *TRE-Tight* promoter in *pTRE-Tight* (Clontech), and then the entire construct was subcloned into the pAAV vector (Stratagene). Recombinant AAV serotype 2 was produced using the pAAV helper free kit (Stratagene) according to the manufacturer's instructions. AAV was also produced commercially by the Gene Therapy Center of the University of North Carolina. The AAV titre was estimated to be $\sim 4 \times 10^{12}$ viral particles ml^{-1} based on serial dilution and blot hybridization analysis. Pseudotyped *ΔG* rabies virus was prepared as previously described[3,54]. The pseudotyped rabies virus titre was estimated to be $\sim 5 \times 10^8$ infectious particles per ml based on the infections of cell line 293-TVA800 by serially diluted virus stocks.

Animal surgery. All animal procedures followed animal care guidelines approved by A-PLAC. To activate Cre in animals carrying a *CreER* transgene, we injected intraperitoneally 0.1–1 mg of tamoxifen (Sigma) dissolved in corn oil into mice around PD10. For trans-synaptic labelling, 0.1–0.3 μl of AAV-*TRE-HTG* was injected into brain at PD21 by using a stereotactic apparatus (KOPF). During surgery, animals were anaesthetized with 65 mg kg^{-1} ketamine and 13 mg kg^{-1} xylazine (Ben Venue Laboratories). For motor cortex injections, the needle was placed 1.5 mm anterior and 1.5 mm lateral from the Bregma, and 0.4 mm from the brain surface. For olfactory cortex injections, see Supplementary Fig. 1b for the stereotactic parameters. After recovery, animals were housed in regular 12 h dark/light cycles with food and water *ad libitum*. Two weeks later, 0.3 μl of pseudotyped rabies virus (Δ*G-mCherry*+EnvA) was injected into the same brain location under anaesthesia. After recovery, animals were housed in a biosafety room for 7 days to allow rabies virus to infect, trans-synaptically spread and express sufficient amount of mCherry to label presynaptic cells. All animals were healthy and their brain structures were normal 7 days after rabies virus infection, confirming non-pathogenicity of ΔG mutant rabies virus.

Tissue processing. Brain tissue was processed according to previously described procedures[55]. To set the common coronal plane among different animals, the cerebellum was cut off and the brain was embedded in the Optimum Cutting Temperature (OCT) compound (Tissue-Tek) with the cut surface facing the bottom of the mould. The brain was adjusted to ensure that the left–right axis was parallel to the section plane. Neither mCherry nor histone–GFP required immunostaining for visualization. In some cases, brain sections were immunostained for better signal preservation according to previously published methods[56] using the following antibodies: chicken anti-GFP (1:500; Aves Labs), rabbit anti-DsRed (1:1,000; Clontech), donkey anti-chicken fluorescein isothiocyanate (FITC) and donkey anti-rabbit Cy3 (1:200; Jackson ImmunoResearch). In most trans-synaptic labelling experiments starting from the olfactory cortex, every one of four sections of the olfactory bulb was immunostained by the free-floating method with goat anti-OCAM (1:100; R&D Systems) and donkey anti-goat Alexa488 (Invitrogen) to label OCAM$^+$ olfactory receptor neuron axons. For immunostaining against GABA, 60-μm free-floating coronal sections were treated with rabbit anti-GABA (1:2,000 in PBS with 0.3% Triton-X100; Sigma) for 48 h. GABA$^+$ cells were visualized with donkey anti-rabbit Cy3 (1:200; Jackson ImmunoResearch). Sections were imaged with a Nikon CCD camera by using a 10× objective or by 1-μm optical sectioning using confocal microscopy (Zeiss 510).

3D reconstruction. To compare distribution of labelled glomeruli (olfactory bulb) and starter cells (AON) across different samples, we needed to map them in a common 3D reference frame. To do this, we first saved manual annotations carried out in Adobe Illustrator in a scalable vector graphics (SVG) format. The SVG file saved all the annotations as an extensible markup language (XML) file describing the ellipses and contours (defined later), making it feasible to accurately parse the information by MATLAB scripts. In the olfactory bulb, we represented all glomeruli as ellipses. We used the centre of mass for each ellipse to define a single point, and calculated the centre of mass of all the points to define the centre of each slice. For the AON, we defined the contour as the boundary between layer I and layer II, which can be clearly distinguished by differences in the density of 4′,6-diamidino-2-phenylindole (DAPI) staining. To define the centre of mass for each contour, we replaced it with a dense series of points and used these points to calculate the centre of mass. Now, each slice is represented by a series of points and the centre of mass contained within an SVG file. To assemble the slices represented by SVG files into a 3D shape, we first aligned the centre of mass for each slice to that of the previous slice to form the cylindrical (*z*-)axis. Then, we refined the alignment by sequentially applying the iterative closest points (ICP) algorithm[56], which can identify the local rotation and translation parameters for each slice to maximize the overlap with the previous slice. Once we had aligned all the slices in a sample to generate a 3D shape, we needed to identify an orientation for the polar axis that could be most reliably identified in different 3D reconstructions. As the olfactory bulb is ellipsoidal, the principle component analysis (PCA) can reliably find a plane that contains the *z*-axis and intersects the 3D shape to maximize the surface of the intersection (plane *m*). We then defined the polar axis to be contained within the plane *m*, perpendicular to the *z*-axis, and pointing in the dorsal direction. For the AON, we approximated the contours of the most posterior slide of the AON as a triangle and calculated the rotation around the *z*-axis that minimizes the distance of the three vertices to those of a standard AON sample. We applied the same rotation to the whole 3D shape. To define the orientation of the polar axis, we used the side of the triangle that connects two of its medial vertices and points in the dorsal direction. Then we defined the polar axis as the line that is parallel to it and that intersects the *z*-axis. Finally, we calculated the volume occupied by each shape and applied a uniform scaling factor to account for different sizes of the anatomical structures in different animals.

All the steps explained earlier were implemented in MATLAB, which ran automatically without human intervention to avoid biasing the registration results. Once we had registered each shape, we used a standard algorithm to extract surfaces from two-dimensional (2D) contours[57] to transform the point cloud into a triangulated mesh that could be saved in the visualization toolkit (VTK)[58] format for visualization and analysis purposes.

We used the following landmarks to map starter cells in the amygdala and piriform cortex (Fig. 3): appearance of the olfactory tubercle (Fig. 3, I); end of the olfactory tubercle (Fig. 3, II); appearance of the hippocampus (Fig. 3, III); and appearance of the dentate gyrus of the hippocampus, on the ventral edge of the cortex (Fig. 3, IV).

Quantitative analyses. For each tracing experiment where we analysed the distribution of labelled glomeruli along the dorsal–ventral axis using mean θ'_{OB} (Fig. 3e), we generated a corresponding random distribution of simulated mean θ'_{OB} (mean $^{sim}\theta'_{OB}$) from *M* glomeruli, where *M* is the number of labelled glomeruli in the injection. To generate this random distribution for each experiment, we randomly selected *M* glomeruli from a given 3D reconstruction model (generated from that injection) and calculated the mean $^{sim}\theta'_{OB}$ value for those randomly selected *M* glomeruli to get the mean $^{sim}\theta'_1$. We then repeated the same simulation 50,000 times to obtain mean $^{sim}\theta'_2$,..., mean $^{sim}\theta'_{50,000}$, and therefore to obtain the range of mean $^{sim}\theta'$ for *M* glomeruli that are randomly distributed throughout the olfactory bulb. Once we obtained distributions for mean $^{sim}\theta'_{OB}$ that corresponded to each injection, we compared the mean $^{sim}\theta'_{OB}$ distribution with the experimental mean θ'_{OB}. If the value for the experimental mean θ'_{OB} was outside of the 95% of the mean $^{sim}\theta'_{OB}$ distribution, we considered the glomerular distribution to be non-random for that sample.

Multiple regression analysis (Fig. 4b) was conducted by using Excel (Microsoft). Data from every experiment in Supplementary Table 1 ($n = 8$ for the AON, $n = 10$ for the piriform cortex using *actin-CreER*) was used for the left part of the Fig. 4b. Data from seven experiments obtained from *GAD2-CreER* in the anterior piriform cortex were used in Fig. 4b, right. The number of labelled mitral cells in the olfactory bulb was set as a dependent variable, Y, and the number of starter cells in layer k ($k = \mathrm{I}, \mathrm{II}, \mathrm{III}$) was set as an independent variable, X_k. The constant was set to zero. Excel then calculated the values of coefficients A_k (shown by red crosses in Fig. 4b) and 95% confidence intervals of A_k based on the student's t-test (shown by grey bars in Fig. 4b). R^2 values for these multiple regression assays were: 0.98 for the AON; 0.96 for the piriform cortex (*actin-CreER*); and 0.97 for the piriform cortex (*GAD2-CreER*) data sets.

To estimate the number of dually labelled glomeruli originating from single starter cells (data Ds in Fig. 4c) in our experimental data, we first simulated a hypothetical number of dually labelled glomeruli originating from single starter cells (Ds) and two independent starter cells (Dt) according to the null hypothesis that mitral cells connect randomly with postsynaptic targets. This situation can be modelled by 'balls and bins': there are 2,000 bins (a bin represents a single glomerulus) and N balls (a ball represents a single trans-synaptic labelling event). N balls were randomly thrown into 2,000 bins, and the number of bins that received more than one ball (that is, glomeruli labelled more than once) was counted. To distinguish Ds from Dt, we further introduced n different colours to the balls, where each colour represented an individual starter cell in the cortex. We assumed that an equal number of balls (N/n) were labelled with n different colours. Each ball was randomly thrown into one of 2,000 bins, and the number of bins containing more than one ball was counted. We separately counted the bins with more than one ball of an identical colour (representing Ds) and the bins with more than one ball of different colours (representing Dt). We fixed the number of bins (glomeruli) to be 2,000, while N and n corresponded to the number of labelled mitral cells and the number of starter cells, respectively, in each experiment. We repeated this simulation 100,000 times for each set of N and n to obtain the simulated distribution of Ds and Dt (we call these 'random Ds' and 'random Dt'). To estimate the Ds components in experimental data (data Ds), we assumed that individual starter cells contributed independently to the labelling (random Dt = data Dt). On the basis of the equation: D (number of observed dually labelled glomeruli) = Ds + Dt, we estimated the data Ds distribution by subtracting the random Dt from observed D (Fig. 4c). Then we determined if there was a significant difference in the distribution of data Ds and random Ds. We considered two distributions to be significantly different if the probability of data Ds > random Ds or data Ds < random Ds exceeded 0.95 (shown by asterisks in Fig. 4c). To accurately count dually labelled glomeruli, samples with more than 200 labelled mitral cells were excluded from this analysis.

49. Urlinger, S. *et al.* Exploring the sequence space for tetracycline-dependent transcriptional activators: novel mutations yield expanded range and sensitivity. *Proc. Natl Acad. Sci. USA* **97,** 7963–7968 (2000).
50. Zong, H., Espinosa, J. S., Su, H. H., Muzumdar, M. D. & Luo, L. Mosaic analysis with double markers in mice. *Cell* **121,** 479–492 (2005).
51. Muzumdar, M. D., Luo, L. & Zong, H. Modeling sporadic loss of heterozygosity in mice by using mosaic analysis with double markers (MADM). *Proc. Natl Acad. Sci. USA* **104,** 4495–4500 (2007).
52. Chung, J. H., Whiteley, M. & Felsenfeld, G. A 5′ element of the chicken β-globin domain serves as an insulator in human erythroid cells and protects against position effect in *Drosophila*. *Cell* **74,** 505–514 (1993).
53. Li, L. *et al.* Visualizing the distribution of synapses from individual neurons in the mouse brain. *PLoS ONE* **5,** e11503 (2010).
54. Wickersham, I. R., Sullivan, H. A. & Seung, H. S. Production of glycoprotein-deleted rabies viruses for monosynaptic tracing and high-level gene expression in neurons. *Nature Protocols* **5,** 595–606 (2010).
55. Espinosa, J. S., Wheeler, D. G., Tsien, R. W. & Luo, L. Uncoupling dendrite growth and patterning: single-cell knockout analysis of NMDA receptor 2B. *Neuron* **62,** 205–217 (2009).
56. Zhang, Z. Iterative point matching for registration of free-form curves and surfaces. *Int. J. Comput. Vis.* **13,** 119–152 (1994).
57. Cong, G. & Parvin, B. Surface reconstruction from sparse fringe contours. *Proc. 4th IEEE Workshop Applicat. Comput. Vis.* **140** (1998).
58. Schroeder, W., Martin, K. & Lorensen, B. *The Visualization Toolkit: An Object-Oriented Approach to 3-D Graphics* (Prentice Hall, 1997).